

# One-Pot Decoration of Graphene with SnO<sub>2</sub> Nanocrystals by an Elevated Hydrothermal Process and Their Application as Anode Materials for Lithium Ion Batteries

Zhen Kong<sup>1</sup>, Dongdong Liu<sup>1</sup>, Xuehua Liu<sup>1</sup>, Aiping Fu<sup>2</sup>, Yiqian Wang<sup>2,3</sup>, Peizhi Guo<sup>1</sup>, and Hongliang Li<sup>1,\*</sup>

<sup>1</sup>*Institute of Materials for Energy and Environment, College of Materials Science and Engineering, Qingdao University, Qingdao 266071, China*

<sup>2</sup>*Laboratory of New Fiber Materials and Modern Textile, Growing Basis for State Key Laboratory, Qingdao University, Qingdao 266071, China*

<sup>3</sup>*College of Physics, Qingdao University, Qingdao 266071, China*

Tin dioxide (SnO<sub>2</sub>), with a high theoretical storage capacity of 782 mAhg<sup>-1</sup>, is a potential alternative anode for rechargeable lithium ion batteries (LIBs). However, its low electronic conductivity and poor stability during cycling (due to a change in volume) hinder its practical applications for energy storage. Composite materials of SnO<sub>2</sub>-nanocrystal-decorated graphene, which show excellent electrochemical characteristics, were prepared using a one-pot elevated hydrothermal method at 250 °C without subsequent carbonization treatment. The effects of graphene, solvent composition, and temperature on the morphology, structure, and electrochemical properties of the SnO<sub>2</sub>/graphene composites were investigated using XRD, SEM, TEM, and N<sub>2</sub> adsorption-desorption techniques. The as-prepared SnO<sub>2</sub>/graphene composites deliver a high initial discharge capacity of 1734.1 mAh g<sup>-1</sup> at 200 mA g<sup>-1</sup> and exhibit a high reversible capacity of 814.7 mAh g<sup>-1</sup> even after 70 cycles at a current density of 200 mA g<sup>-1</sup>. The composites also exhibit a high rate capability of 596 mAh g<sup>-1</sup> at 2000 mA g<sup>-1</sup>, indicating a long cycle life and promising capability when used as anode materials for lithium ion batteries and suggesting that SnO<sub>2</sub>/graphene composites have wide application prospects in LIBs.

**Keywords:** Tin Dioxide, Graphene, Elevated Hydrothermal Synthesis, Anode Material, Lithium Ion Battery.

## 1. INTRODUCTION

Lithium ion batteries (LIBs) are the most popular energy storage devices for applications in portable electronics, electric vehicles, and hybrid electric vehicles owing to their relatively high energy density and power density.<sup>1,2</sup> However, the commercially used graphite anode has a limited lithium storage capacity (372 mAh g<sup>-1</sup>).<sup>3</sup> Developing alternative anode materials with a superior reversible capacity, higher rate capability, long cycle life, and low cost has therefore been a focus of extensive research. Various materials, including metal oxides, have been studied as alternative anode materials for LIBs.<sup>4</sup> SnO<sub>2</sub> is considered a promising substitute for graphite due to its attractive

theoretical capacity (782 mAh g<sup>-1</sup>), low discharge potential for Li alloying (<1.5 V), and low cost.<sup>5,6</sup> Yet the practical utilization of SnO<sub>2</sub>-based material is hindered by its clearly diminished capacity induced by intensive volume change and particle aggregation along with repeated alloying/dealloying processes.<sup>7</sup> Several efforts have aimed to eliminate the influences of volume changes and to enhance the cycling performance of the SnO<sub>2</sub> electrode. One such attempt is called structure and morphology control, using reasonable design and synthesis of SnO<sub>2</sub> with a novel shape and porous/hollow properties on the nano-dimension.<sup>8</sup> Such an effect could withstand the strong volume change during charge and discharge processes.<sup>9</sup> Another scheme is to form a composite with carbon, which can effectively cushion the stresses of SnO<sub>2</sub> size changes

\*Author to whom correspondence should be addressed.

during the lithiation and delithiation processes to maintain good electrical conductivity in the anode.<sup>10,11</sup> As a fashionable two-dimensional carbon species, graphene has been exploited as matrices for composite fabrication due to its excellent conductivity, superior mechanical characteristics, and large surface area.<sup>12</sup> As a result, SnO<sub>2</sub>/graphene composites have been prepared via *in-situ* growth of SnO<sub>2</sub> particles on the surface of graphene, showing high reversible capacities and enhanced cycle performance. For example, Prabakar et al. reported that SnO<sub>2</sub>/graphene composites exhibited a capacity of 872 mA h g<sup>-1</sup> after 200 cycles at a current density of 100 mA h g<sup>-1</sup>.<sup>13</sup> Li et al. found that SnO<sub>2</sub>-carbon-graphene nanoparticles demonstrated a stable reversible capacity of 720 mA h g<sup>-1</sup> after 70 cycles at a current density of 100 mA h g<sup>-1</sup>.<sup>14</sup> However, most syntheses require subsequent calcination.<sup>15</sup>

To circumvent the aforementioned issue associated with the fabrication of SnO<sub>2</sub>-related composites, we explored a one-pot hydrothermal synthesis at an elevated temperature of 250 °C to the fabrication of SnO<sub>2</sub>-encapsulated graphene composite materials (i.e. SnO<sub>2</sub>/Graphene, and is abbreviated to SnO<sub>2</sub>/G). During the elevated hydrothermal process, high pressure was induced in the autoclave due to the temperature elevation, and the formation of SnO<sub>2</sub> nanocrystals and their decoration onto the surface of graphene layers were deduced *in-situ*. The SnO<sub>2</sub>/G composite delivered a high reversible capacity of 814 mAh g<sup>-1</sup> even after 70 cycles at a current density of 200 mA g<sup>-1</sup> and demonstrated good cycling stability. In comparison with the pristine SnO<sub>2</sub> and graphene, respectively, the composite material showed a synergistic effect between them. This work also attempted to illustrate the effect (e.g., the solvent used in the hydrothermal process) on the properties of the resultant SnO<sub>2</sub>/G composites.

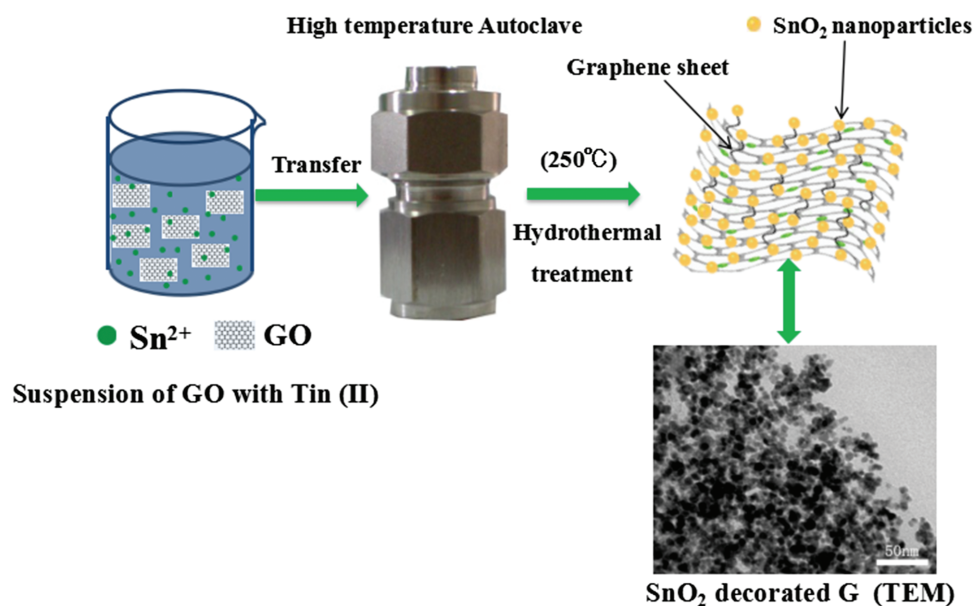
## 2. EXPERIMENTAL DETAILS

### 2.1. Materials

Tin(II) oxalate, urea, and ethylene glycol (Sinopharm Chemical Reagent Co., Ltd., Shanghai, China) were all AR grade and used without further purification. Graphene oxide (GO) powder, kindly provided by the sixth element (Changzhou) Ltd., was used as received.

### 2.2. Synthesis of SnO<sub>2</sub>/G Composites

The SnO<sub>2</sub>/graphene composites were synthesized via a one-pot high-temperature hydrothermal route. Typically, a solution (5 mL) was prepared by dissolving the Tin(II) oxalate precursor and urea at a molar ratio of 1:5 in the solvent. Then, 13 mg of GO was added into the solvent followed by ultrasonic irradiation for 1 h. The resultant suspension was transferred into a homemade stainless autoclave (8 mL), which was then heated to 250 °C in a thermostat oven for 15 h. After a natural cooling process, the black product was thoroughly washed with deionized water thrice and dried overnight in a vacuum oven at 80 °C. Three kinds of solvents viz. pure deionized water, a mixture of deionized water and ethylene glycol with a volume ratio of 1:1 and that with a volume ratio of 1:2 were adopted in the sample preparation for SnO<sub>2</sub>/G-1, SnO<sub>2</sub>/G-2, and SnO<sub>2</sub>/G-3, respectively. An illustration of the formation process of the SnO<sub>2</sub>/G composites is depicted in Scheme 1. For comparison, pristine SnO<sub>2</sub> nanoparticles were prepared using the same procedure as SnO<sub>2</sub>/G-2 without adding graphene. Similarly, a graphene solid was obtained in the absence of Tin(II) oxalate. As a control experiment, the SnO<sub>2</sub>/G-4 composite was also prepared using the traditional solvothermal method at 180 °C for 15 h using GO and Tin(II) oxalate as precursors.



**Scheme 1.** Illustration of the formation process of the SnO<sub>2</sub>/G composites.

### 2.3. Characterization of SnO<sub>2</sub>/Graphene Composites Electrodes

X-ray diffraction patterns were recorded on a Rigaku Ultima IV X-ray diffractometer with Cu-K $\alpha$  radiation ( $\lambda = 0.15418$  nm) at the scan rate of 5 degree min<sup>-1</sup> with a scan range from 10° to 90°. Fourier transform infrared spectra were collected between the wavelengths of 400–4000 cm<sup>-1</sup> with a Nicolet 5700 spectrophotometer using pressed KBr pellets. Nitrogen adsorption/desorption measurement were carried out using an Autosorb-IQ-MP/XR analyzer at -196 °C (Quantachrome). The specific surface areas were estimated with the Brunauer-Emmett-Teller (BET) method with N<sub>2</sub> adsorption data in the relative pressure range of  $P/P_0 = 0.05$ –0.35. Pore size distributions were derived using the Barrett-Joyner-Halenda (BJH) model based on the desorption data of the N<sub>2</sub> isotherms. The thermogravimetric analysis was performed with a Mettler Toledo TGA-2 thermal gravimetric analyzer under an air atmosphere with a heating rate of 5 °C min<sup>-1</sup>. Morphology and structure were examined by a JEOL JSM-7800F field emission scanning electron microscope (FESEM) and a JEOL JEM-2100 plus transmission electron microscope (TEM). Raman spectra were recorded on a Renishaw in Via-Reflex confocal Raman microscope with an excitation wavelength of 532 nm.

### 2.4. Electrochemical Preparation and Characterization

The electrochemical properties of the SnO<sub>2</sub>/G electrodes were measured by assembling them into coin cells (type CR2016). Working electrodes were fabricated by mixing the electrode materials, Super P carbon black, and polyvinylidene difluoride (PVDF) binder in *N*-methyl pyrrolidone with a weight ratio of 80:10:10. The slurry was then coated on Cu foil before being dried at 110 °C for 10 h to remove the water and solvent. Pure lithium metal foil was used as the counter-electrode. A LiPF<sub>6</sub>

solution (1 M) in a mixture of ethylene carbonate, ethylene methyl carbonate, and diethyl carbonate (1:1:1 by volume) was utilized as the electrolyte. The cells were assembled in an Ar-filled glove box (oxygen and moisture of less than 1 ppm) using Celgard 2400 film as the separator. The cells were galvanostatically charged and discharged in the voltage range of 0.01–3.0 V on a battery test system (LAND-2001A; Land Electronic Co., Ltd., Wuhan). Cyclic voltammetry (CV) curves were collected on a CHI760D electrochemical working station at a scan rate of 0.2 mv s<sup>-1</sup>. Electrochemical impedance spectra (EIS) were also recorded on the CHI760D electrochemical working station by applying a sine wave with an amplitude of 10 mV over a frequency range of 100 kHz–10 mHz.

## 3. RESULTS AND DISCUSSION

### 3.1. XRD

The crystal structure of the prepared SnO<sub>2</sub>/graphene composites was revealed by X-ray diffraction (XRD) and the results are depicted in Figure 1. The main peaks observed correspond to the (110), (101), (201), and (301) planes of the SnO<sub>2</sub> crystal (JCPDS No. 41-1445), respectively, which can be indexed to the tetragonal rutile SnO<sub>2</sub> phase. When no graphene was added during the experiment, additional peaks at  $2\theta = 29.8, 33.22, 50.66,$  and  $57.34$  appeared. These peaks can be assigned to the characteristic planes of (101), (110), (112), and (211) of the SnO crystal (JCPDS No. 06-0395), suggesting that graphene can induce the transformation of SnO into SnO<sub>2</sub> due to the large number of oxygen-containing functional groups on the graphene surface. All the typical peaks are clearly broadened, demonstrating that the SnO<sub>2</sub> particle size is small. No obvious diffraction peaks of graphene can be observed, implying that the stacking of graphene sheets is disordered in these composites.<sup>16</sup>

### 3.2. FTIR Spectra

Figure 2 shows the FT-IR spectra of G, SnO<sub>2</sub>/G-1, SnO<sub>2</sub>/G-2, and SnO<sub>2</sub>/G-3 composites measured in the

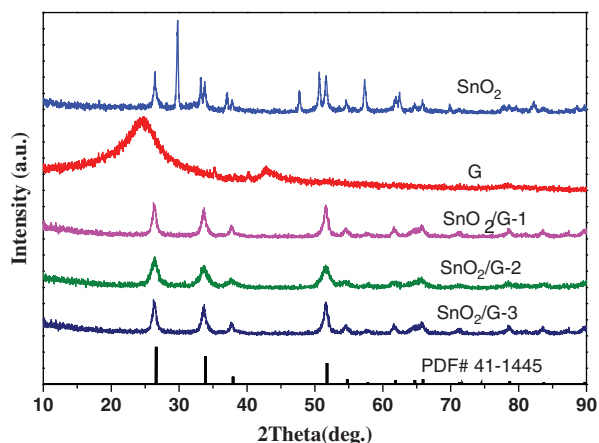


**Figure 1.** XRD patterns of the pristine SnO<sub>2</sub>, G and SnO<sub>2</sub>/G-1, SnO<sub>2</sub>/G-2 and SnO<sub>2</sub>/G-3.

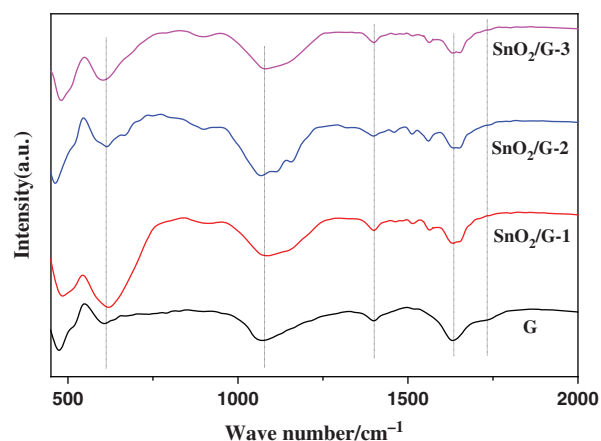


**Figure 2.** FTIR spectra of G, SnO<sub>2</sub>/G-1, SnO<sub>2</sub>/G-2 and SnO<sub>2</sub>/G-3.

wavelength range of 400–2500 cm<sup>-1</sup>. As depicted in the graphs, the characteristic peaks of graphene also appear in these SnO<sub>2</sub>/G composites: the peak at 1070 cm<sup>-1</sup> can be attributed to the skeletal C–O stretching vibration; the peak at 1400 cm<sup>-1</sup> can be designated as the skeletal C–H stretching vibration; and the peak at 1630 cm<sup>-1</sup> can be assigned to the C=C bending vibrations of graphene.<sup>4</sup> The weak peak at 1731 cm<sup>-1</sup> was ascribed to the C=O stretching vibration. These results further confirm that conductive graphene existed in the composites after the elevated hydrothermal process. The spectra of the SnO<sub>2</sub>/G composites show the typical Sn–O stretching vibration at ~612 cm<sup>-1</sup>, confirming the presence of SnO<sub>2</sub>.<sup>17</sup>

### 3.3. SEM and TEM Measurements

The morphology of the as-prepared SnO<sub>2</sub>/G composites was investigated using scanning electron microscopy (SEM) and transmission electron microscopy (TEM). Figure 3 presents typical SEM images of pristine SnO<sub>2</sub> and SnO<sub>2</sub>/G composites. As shown, the control sample of pristine SnO<sub>2</sub> (mixture containing some SnO nanoparticles) show a rod-like morphology with some flakes (Fig. 3(A)). SnO<sub>2</sub>/G composites exhibit a curled morphology consisting of a thin, wrinkled structure, where nanosized SnO<sub>2</sub> particles are uniformly deposited on the surface of the graphene sheets and no isolated SnO<sub>2</sub> particles appear outside the graphene sheets. The size of the SnO<sub>2</sub> nanoparticles was observed in Figure 3; they are small with diameters ranging from 5–20 nm. The SEM images of

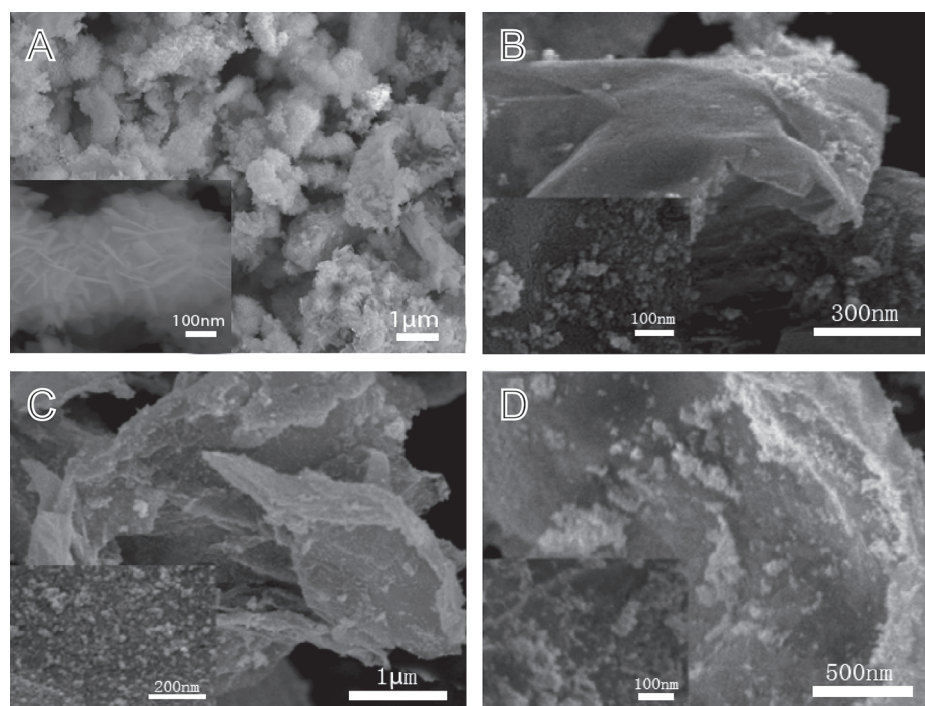
SnO<sub>2</sub>/G-2 (Fig. 3(C)) exhibit a more uniform deposition of SnO<sub>2</sub> nanoparticles on the surface of GO compared to the sample of SnO<sub>2</sub>/G-1 (Fig. 3(B)) and SnO<sub>2</sub>/G-3 (Fig. 3(D)).

Image A and images B–D in Figure 4 show the TEM images of graphene and the SnO<sub>2</sub>/G composites, respectively. The image of pristine graphene substrate displays a clearly layered structure that is stacked and wrinkled. The TEM image of SnO<sub>2</sub>/G-2 (Fig. 4(C)) confirms that SnO<sub>2</sub> nanoparticles with diameters ranging from 10–20 nm were anchored uniformly on the surface of the graphene sheets after the one-pot solvothermal treatment at 250 °C, consistent with the SEM results. TEM images of SnO<sub>2</sub>/G-1 (Fig. 4(B)) and SnO<sub>2</sub>/G-3 (Fig. 4(D)) show unevenly sized SnO<sub>2</sub> particles with most SnO<sub>2</sub> particles agglomerated and distributed irregularly on the surface of graphene sheets compared to the SnO<sub>2</sub>/G-2 sample (Fig. 4(C)).

The above results suggest that GO acts as effective heterogeneous nucleation and growth sites for the formation of SnO<sub>2</sub> nanoparticles during the one-pot hydrothermal synthesis of the composites. The compact contact between the SnO<sub>2</sub> particles and graphene sheets can effectively facilitate electron transfer from GO to the SnO<sub>2</sub> phase during the charge and discharge process.

### 3.4. Nitrogen Adsorption–Desorption Measurements

To investigate the porosity and specific surface area of the SnO<sub>2</sub>/G-2 composite and the SnO<sub>2</sub> nanoparticles, N<sub>2</sub> adsorption/desorption experiments were performed; the isotherms and corresponding pore size distribution curves



**Figure 3.** SEM images of SnO<sub>2</sub> (A), SnO<sub>2</sub>/G-1 (B), SnO<sub>2</sub>/G-2 (C) and SnO<sub>2</sub>/G-3 (D).

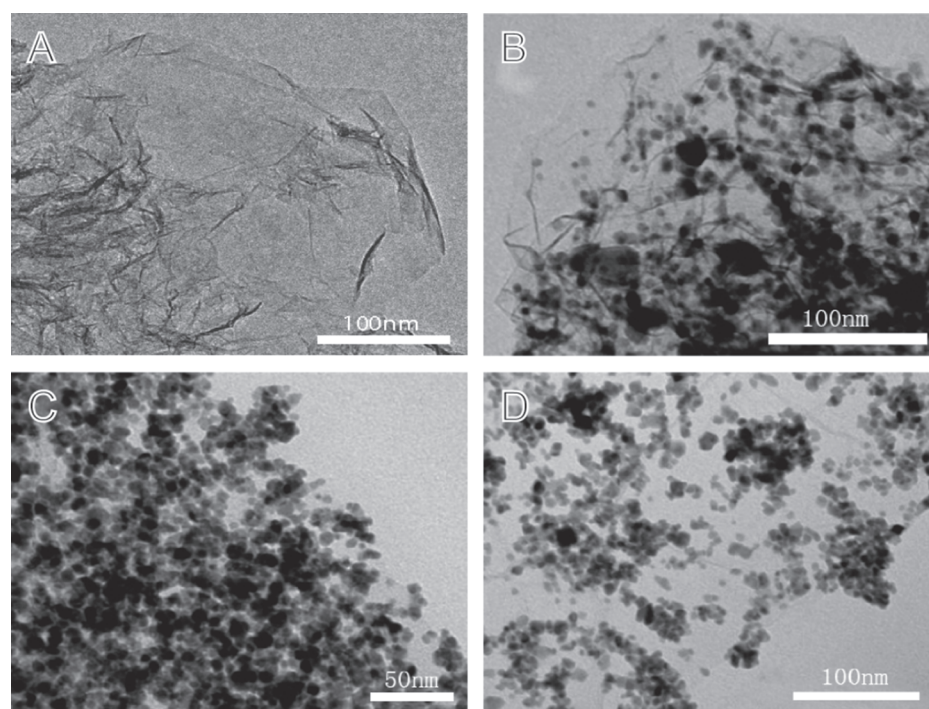


**Figure 4.** TEM images of G (A), SnO<sub>2</sub>/G-1 (B), SnO<sub>2</sub>/G-2 (C) and SnO<sub>2</sub>/G-3 (D).

are depicted in Figure 5. The isotherms of SnO<sub>2</sub>/G-2 composite are close to the type-IV curve with an H3 hysteresis loop, indicating a mesoporous structure.<sup>18</sup> The size of the hysteresis loop is associated with the volume and connectivity of the pores. The BET-specific surface area and total pore volume of each sample are shown in Table I.

Table I lists the surface area values for SnO<sub>2</sub>/G-1 (69.9 m<sup>2</sup> g<sup>-1</sup>) and SnO<sub>2</sub>/G-3 (82.9 m<sup>2</sup> g<sup>-1</sup>), which are smaller than that of SnO<sub>2</sub>/G-2 (100.5 m<sup>2</sup> g<sup>-1</sup>) but larger than that of pure SnO<sub>2</sub> (19.08 m<sup>2</sup> g<sup>-1</sup>). The large specific surface area of SnO<sub>2</sub>/G composites can be attributed to the integration of graphene sheets with SnO<sub>2</sub> nanoparticles and the formation of a porous structure with more

small, connected particles during the hydrothermal process. The higher specific surface area of SnO<sub>2</sub>/G-2 compared to SnO<sub>2</sub>/G-1 and SnO<sub>2</sub>/G-3 can be attributed to the size effect of the SnO<sub>2</sub> nanoparticles, which are smaller in SnO<sub>2</sub>/G-2 than in SnO<sub>2</sub>/G-1 and SnO<sub>2</sub>/G-3. Furthermore, total pore volumes of 0.23, 0.21, and 0.20 cm<sup>3</sup> g<sup>-1</sup> were estimated for SnO<sub>2</sub>/G-1, SnO<sub>2</sub>/G-2, and SnO<sub>2</sub>/G-3 samples, respectively, all of which are larger than that of pristine SnO<sub>2</sub> (0.084 cm<sup>3</sup> g<sup>-1</sup>). The large BET-specific surface area and pore volume for the SnO<sub>2</sub>/G-2 composites could provide more locations and channels for rapid Li ion insertion/extraction into the electrode material. In addition, the porous structure can not only benefit the diffusion of the

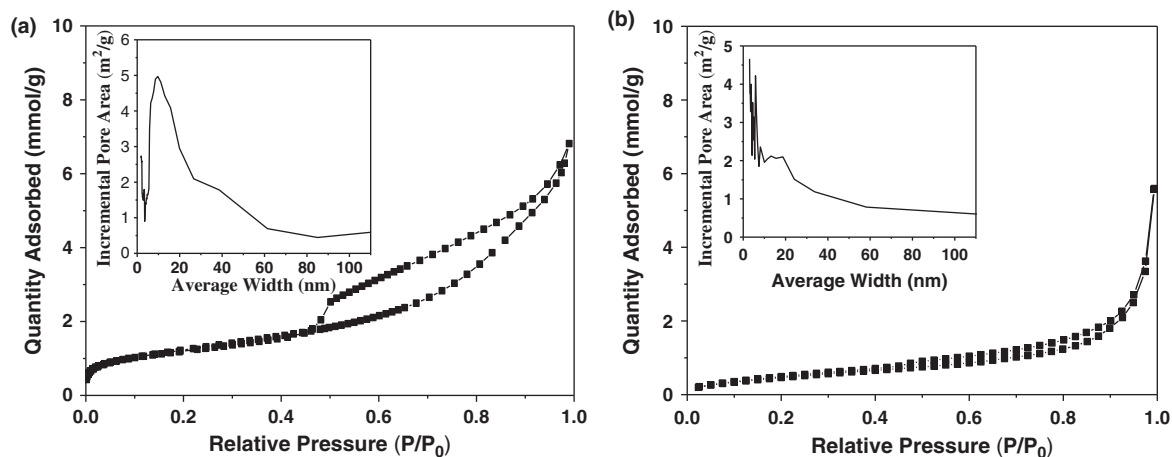


**Figure 5.** The nitrogen adsorption–desorption isotherms and BJH pore size distribution curves (inset) of (a) SnO<sub>2</sub>/G-2 composites and (b) SnO<sub>2</sub>.

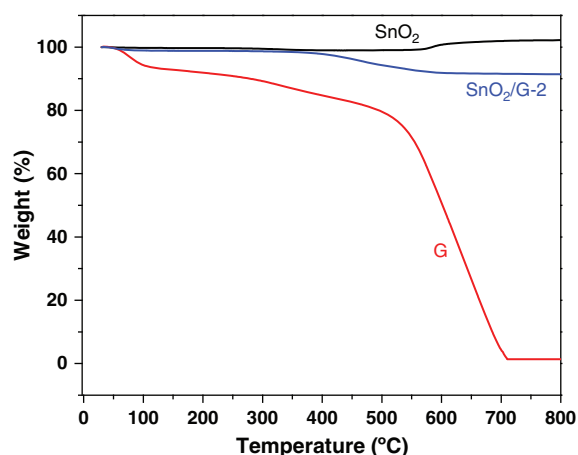
**Table I.** BET specific surface area and pore volumes of SnO<sub>2</sub> and the SnO<sub>2</sub>/G composites.

	SnO <sub>2</sub>	SnO <sub>2</sub> /G-1	SnO <sub>2</sub> /G-2	SnO <sub>2</sub> /G-3
BET surface area (m <sup>2</sup> g <sup>-1</sup> )	19.08	69.9	100.5	82.9
Pore volume (cm <sup>3</sup> g <sup>-1</sup> )	0.084	0.23	0.21	0.20

Li ion but also accommodate volume changes during the alloying reaction to maintain the structural integrity of the SnO<sub>2</sub> particles.<sup>6, 10, 19</sup>

### 3.5. Thermal Analysis

Figure 6 shows the TGA curves of the as-prepared SnO<sub>2</sub>/G-2 composite, pristine SnO<sub>2</sub> particles, and pure G, respectively. TGA was performed in air in a temperature range from room temperature to 800 °C at a rate of 5 °C min<sup>-1</sup>. As shown in the TGA curve of SnO<sub>2</sub>/G-2 composite, a weight loss of 1.2 wt.% between room temperature and 195 °C can be attributed to the evaporation of adsorbed moisture. From 195 °C to 380 °C, there is no obvious weight loss can be observed. While a dramatic weight loss occurred in between 380 to 580 °C, which can be ascribed to the burning of G in the composite. For pristine SnO<sub>2</sub> a weight gain happened after 400 °C, which can be attributed to the conversion of SnO into SnO<sub>2</sub>. For pure G, a slight weight lost can be observed from 80 to 530 °C. However, it showed a drastic weight loss from 530 to 700 °C due to the burning out of graphene. The tight adherence of SnO<sub>2</sub> on the surface of the graphene sheets retards the oxidation rate of graphene, resulting in a different temperature range of weight loss between pristine G and the SnO<sub>2</sub>/G-2 composite. The content of SnO<sub>2</sub> in the SnO<sub>2</sub>/G-2 composite (approximately 91.4 wt.%) was calculated based on the TGA curve. Similarly, the content of SnO<sub>2</sub> in SnO<sub>2</sub>/G-1 and SnO<sub>2</sub>/G-3 composites were estimated to be 89.2 wt.% and 85.7 wt.%, respectively. The detailed mass ratios of SnO<sub>2</sub> and graphene in these SnO<sub>2</sub>/G composites are shown in Table II.

**Figure 6.** TGA curves of pristine G, pure SnO<sub>2</sub> and SnO<sub>2</sub>/G-2 composite.**Table II.** Contents of SnO<sub>2</sub> and graphene for these SnO<sub>2</sub>/G composites.

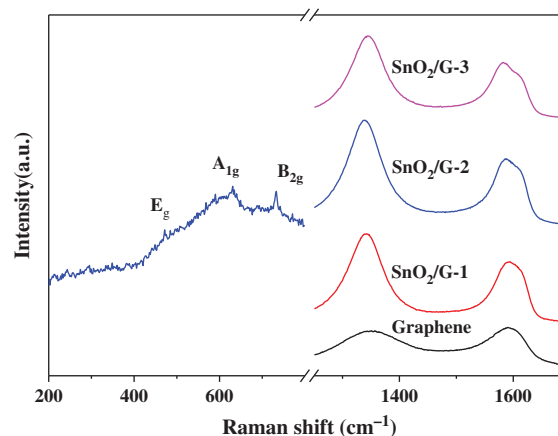
Sample	SnO <sub>2</sub> (wt%)	Graphene (wt%)
SnO <sub>2</sub> /G-1	89.2	10.8
SnO <sub>2</sub> /G-2	91.4	8.6
SnO <sub>2</sub> /G-3	85.7	14.3

### 3.6. Raman Spectra

As a versatile tool for the characterization of carbonaceous materials, Raman spectroscopy has been applied to the investigation of graphene and SnO<sub>2</sub>/G composites. The Raman spectra of graphene, SnO<sub>2</sub>/G-1, SnO<sub>2</sub>/G-2, and SnO<sub>2</sub>/G-3 composites in this study are shown in Figure 7. The G-band at 1340 cm<sup>-1</sup> corresponds to the sp<sup>2</sup> hybridized carbon, while the D-band around 1593 cm<sup>-1</sup> originates from the disordered carbon.<sup>4, 20, 21</sup> The intensity ratios between the D-band and G-band ( $I_D/I_G$ ) for graphene in the three SnO<sub>2</sub>/G composites are much larger (1.44, 1.61, and 1.51, respectively) compared to the GO (1.05), implying a decrease in the mean size of the sp<sup>2</sup>-conjugated domains in the graphene layers given the disposition of SnO<sub>2</sub> nanoparticles.<sup>22</sup> Additionally, three weak peaks appear at 471, 630, and 732 cm<sup>-1</sup> in the low-frequency region of the Raman spectrum of SnO<sub>2</sub>/G-2, which can be assigned to the E<sub>g</sub>, A<sub>1g</sub>, and B<sub>2g</sub> modes, respectively, of rutile-type SnO<sub>2</sub>.<sup>23, 24</sup> Therefore, the Raman spectra again demonstrate the presence of SnO<sub>2</sub> in the composites.

### 3.7. Electrochemical Properties

The electrochemical performance of the SnO<sub>2</sub>/G composites and SnO<sub>2</sub> were investigated via CV measurements and a galvanostatic charge/discharge method. The CV of the SnO<sub>2</sub>/G-2 composites was performed over the potential range of 0.01–3.0 V at a scan rate of 0.2 mV s<sup>-1</sup> (Fig. 8(A)). In the first cycle, an obvious cathodic peak appears at 0.83 V, corresponding to the transformation of SnO<sub>2</sub> to metallic Sn (SnO<sub>2</sub> + 4Li<sup>+</sup> + 4e<sup>-</sup> → Sn + 2Li<sub>2</sub>O)

**Figure 7.** Raman spectra of graphene, SnO<sub>2</sub>/G-1, SnO<sub>2</sub>/G-2 and SnO<sub>2</sub>/G-3.

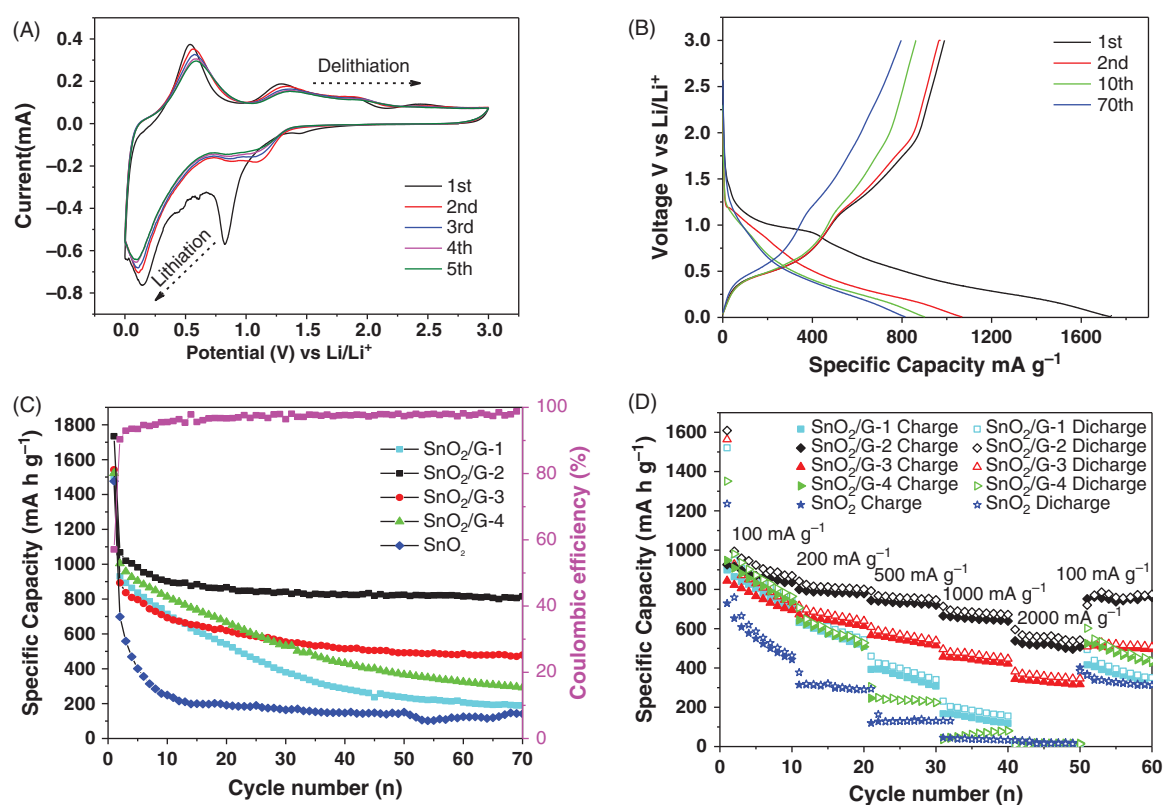


**Figure 8.** (A) First five cycles of the CV curves of the SnO<sub>2</sub>/G-2 composites. (B) The 1st, 2nd, 10th and 70th discharge–charge profiles of the SnO<sub>2</sub>/G-2 composites at a current of 200 mA g<sup>-1</sup>. (C) Cycling stability of bare SnO<sub>2</sub> and SnO<sub>2</sub>/G composites at a current of 200 mA g<sup>-1</sup> and the coulombic efficiency of SnO<sub>2</sub>/G-2 composites. (D) Multi-rate capabilities of bare SnO<sub>2</sub> and SnO<sub>2</sub>/G composites at currents between 100–2000 mA g<sup>-1</sup>.

and the establishment of the solid electrolyte interface (SEI) layer ( $\text{Li}^+ + e^- + \text{electrolyte} \rightarrow \text{SEI}$ ). Another strong reduction peak centrally located at about 0.14 V can be ascribed to the lithiation process of Sn associating with the formation of  $\text{Li}_x\text{Sn}$  ( $\text{Sn} + x\text{Li}^+ + xe^- \rightarrow \text{Li}_x\text{Sn}$ ) alloys.<sup>5</sup> During the anodic sweep, anodic peaks at 0.54 and 1.29 V are also attributed to the delithiation process of  $\text{Li}_x\text{Sn}$  and partial oxidation of Sn to SnO<sub>2</sub>, respectively.<sup>10</sup> The difference between the first and subsequent cathodic sweeps is mainly due to irreversible electrochemical reactions,<sup>25</sup> corresponding to capacity loss during the first cycle. The peak positions and intensities of all the redox couples show no obvious change from the 2nd to the 5th cycles, indicating good reversibility of Li<sup>+</sup> storage in the electrode made of the composite.

The electrochemical cycling performance of the SnO<sub>2</sub>/G composite electrodes was evaluated using deep charge/discharge galvanostatic cycling from 3 to 0.05 V (Figs. 8(B–D)). Figure 8(B) depicts the discharge/charge curves of the SnO<sub>2</sub>/G-2 composites at the 1st, 2nd, 10th, and 70th cycles with a current density of 200 mA g<sup>-1</sup>. The poorly defined plateau regions are consistent with the broad peaks shown in the CV profiles. In the first cycle, the discharge and charge capacities are 1734.1 and 989.8 mAh g<sup>-1</sup> with an initial Coulombic efficiency of 57.1%. The initial irreversibility of the composites may

be due to the presence of SEI film and the transformation of SnO<sub>2</sub> to Sn.<sup>26,27</sup> The Coulombic efficiency soared to 90.3% in the second cycle, indicating the recovery of high reversibility. The Coulombic efficiency improves significantly in the subsequent cycles and attains a stable value >95.6% after the 10th cycle. After 70 cycles, the SnO<sub>2</sub>/G-2 composites still exhibit a high reversible discharge capacity of 814.7 mAh g<sup>-1</sup>, implying robust structural stability upon cycling.

Figure 8(C) shows the charge/discharge cycling performance of bare SnO<sub>2</sub>, SnO<sub>2</sub>/G-1, SnO<sub>2</sub>/G-2, SnO<sub>2</sub>/G-3, and SnO<sub>2</sub>/G-4 composites at a current density of 200 mA g<sup>-1</sup>. All these samples demonstrate high discharge capacities of 1476, 1505, 1734, 1542, and 1522 mAh g<sup>-1</sup> in the first cycle, respectively, before decreasing to 690, 886, 990, 823, and 963 mAh g<sup>-1</sup> in subsequent cycles. The difference in the discharge capacity between the first and second cycles was attributed to their reversible reactions as discussed previously. Clearly, the SnO<sub>2</sub>/G-2 electrode shows significantly improved cyclic capacity retention compared with bare SnO<sub>2</sub> and the other SnO<sub>2</sub>/G composites. After the first cycle, the discharge capacity and charge capacity drop slightly, leading to a rapid increase in Coulombic efficiency to a stable value close to 100%. At the end of the 70th charge/discharge cycle, a reversible discharge capacity of 814.7 mAh g<sup>-1</sup> can still be retained for

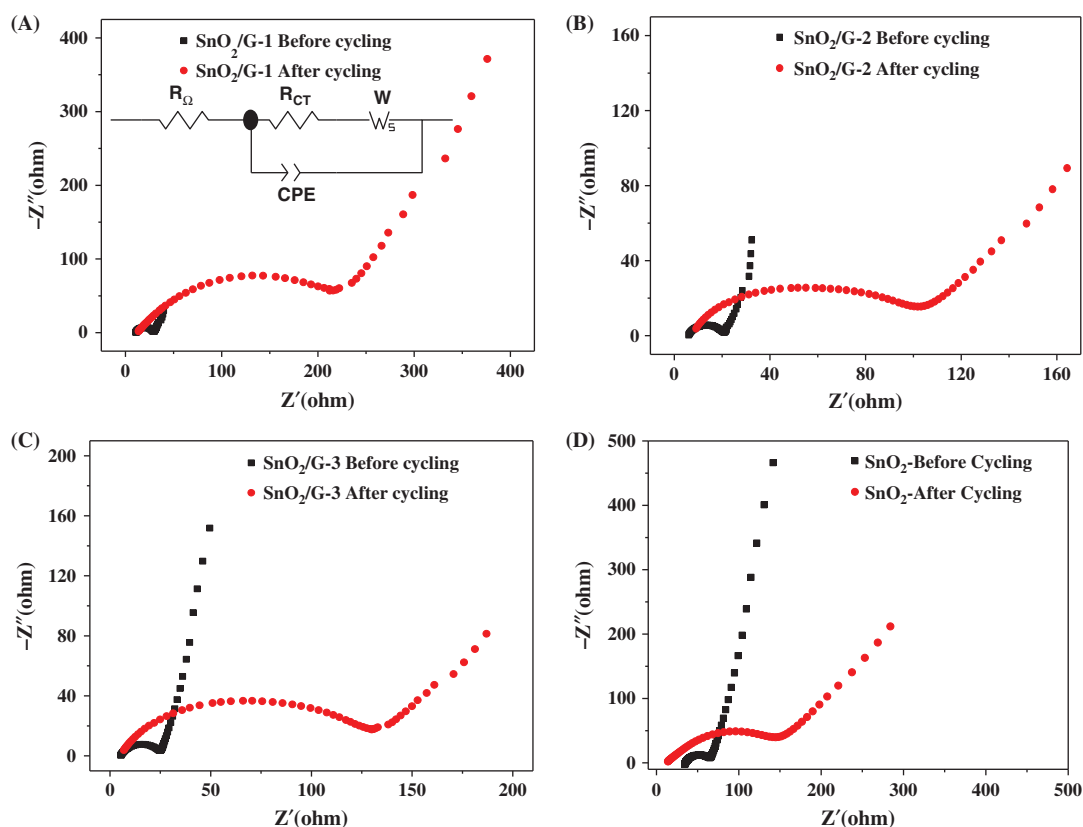


**Figure 9.** Nyquist plots of (A) SnO<sub>2</sub>/G-1, (B) SnO<sub>2</sub>/G-2, (C) SnO<sub>2</sub>/G-3 composites and (D) SnO<sub>2</sub>.

the SnO<sub>2</sub>/G-2 composite, while the bare SnO<sub>2</sub>, SnO<sub>2</sub>/G-1, SnO<sub>2</sub>/G-3, and SnO<sub>2</sub>/G-4 can only deliver a poor capacity of 144, 189, 499, and 292 mAh g<sup>-1</sup> after the same cycles. The excellent electrochemical performance of SnO<sub>2</sub>/G-2 can be attributed to their large specific surface areas, which facilitate electrolyte diffusion and intercalation of the Li ions into the active material.<sup>28</sup>

To better understand the electrochemical behavior of bare SnO<sub>2</sub> and the studied SnO<sub>2</sub>/G samples under various current densities, multi-rate capability performances were studied, the results of which are presented in Figure 8(D). The sample of SnO<sub>2</sub>/G-2 delivers discharge capacities of 1609, 842, 793, 714, and 596 mAhg<sup>-1</sup> at current densities of 100, 200, 500, 1000, and 2000 mA g<sup>-1</sup>, respectively. Obviously, these values are much larger compared to those of bare SnO<sub>2</sub>, SnO<sub>2</sub>/G-1, SnO<sub>2</sub>/G-3, and SnO<sub>2</sub>/G-4 at the corresponding current densities.<sup>29,30</sup> When the current density is retraced to 100 mA g<sup>-1</sup> after 50 cycles at ultra-fast charge-discharge rates (100–2000 mA g<sup>-1</sup>), the initial capacities reappear (about 786 mA h g<sup>-1</sup>) for SnO<sub>2</sub>/G-2 composites, indicating excellent integrity of the composite electrode.<sup>31</sup> This unusual cycling stability at a fast charge-discharge rate can be ascribed to the novel structure of the SnO<sub>2</sub>/G-2 composites: (1) the small particle size and uniform distribution of SnO<sub>2</sub> on the graphene layer can enhance the physical connection and electrical contact of SnO<sub>2</sub> with the 2D conductive substrate; and (2) the porous

graphene matrix acts as a buffer to banish the volume change induced by the alloying of Li<sup>+</sup> with SnO<sub>2</sub> particles.

EIS was employed to assess the electrochemical behaviors of the SnO<sub>2</sub>/G composites and SnO<sub>2</sub> electrodes; results are depicted in Figure 9. The Nyquist plots were fitted by the equivalent circuit as presented in the inset of Figure 9(A), where R<sub>Ω</sub> represents the ohm resistance (total resistance of the electrolyte, separator, and electrical contacts); R<sub>CT</sub> and CPE represent the charge transfer resistance and the double layer capacitance, respectively; and W represents the Warburg impedance, reflecting the solid-state diffusion of Li ions into the bulk of the active materials. As indicated in Figure 9, the diameters of the semicircles for all electrodes increase after cycling compared to before cycling, presumably due to the structural evolution of the composites or the increase of the SEI film during the charge/discharge processes. For the SnO<sub>2</sub>/G-2 electrode, the charge transfer resistance (R<sub>CT</sub>), as measured by the size of the semicircular arc that encompasses the high-middle frequency response, is much smaller than that of the SnO<sub>2</sub>, SnO<sub>2</sub>/G-1, and SnO<sub>2</sub>/G-3 composites after the charge/discharge cycling test.<sup>32</sup> The compact contact of graphene with SnO<sub>2</sub> nanoparticles and its conducting effect of graphene might describe the lower R<sub>CT</sub> value of SnO<sub>2</sub>/G-2, while the homogenous dispersing and anchoring effects of SnO<sub>2</sub> particles on the carbon sheets can explain the smaller changes in R<sub>CT</sub> during cycling. These

EIS results clearly demonstrate the enhanced electrochemical performance of SnO<sub>2</sub>/G composite electrodes.<sup>33,34</sup>

#### 4. CONCLUSIONS

SnO<sub>2</sub>/graphene composites with good electrochemical properties have been prepared via a one-pot hydrothermal synthesis method at an elevated temperature using an organic tin salt as precursor. Benefitting from the large specific surface area and unique porous structure of the derived SnO<sub>2</sub>-encapsulated graphene composites (SnO<sub>2</sub>/G), the composite prepared in a mixture solvent of deionized water/ethylene glycol with a volume ratio of 1:1 showed superior electrochemical properties and a capacity of 814.7 mAh g<sup>-1</sup> at 200 mA g<sup>-1</sup> for 70 cycles. The enhanced rate capability of the composite electrode material is ascribed to the improved electronic conductivity and the enhanced volume accommodation ability of the graphene substrate. This work should narrow the gap between pure research and practical application of SnO<sub>2</sub>-based materials for LIBs.

**Acknowledgments:** This work is supported by the Double First Class University Construction of Shandong Province, the Taishan Scholars Advantageous and Distinctive Discipline Program of Shandong Province for supporting the research team of energy storage materials, and Qingdao Basic and Applied Research Project (15-9-1-56-jch). Y. Wang would like to thank the financial support from the Top-notch Innovative Talent Program of Qingdao City (Grant no.: 13-CX-8).

#### References and Notes

1. M. Armand and J. M. Tarascon, *Nature* 451, 652 (2008).
2. M. S. Whittingham, *Chem. Rev.* 104, 4271 (2004).
3. D. X. Wang, A. P. Fu, H. L. Li, Y. Q. Wang, P. Z. Guo, J. Q. Liu, and X. S. Zhao, *J. Power. Sources* 285, 469 (2015).
4. L. Y. Jing, A. P. Fu, H. L. Li, J. Q. Liu, P. Z. Guo, Y. Q. Wang, and X. S. Zhao, *RSC Adv.* 4, 59981 (2014).
5. W. M. Zhang, J. S. Hu, Y. G. Guo, S. F. Zheng, L. S. Zhong, W. G. Song, and L. J. Wan, *Adv. Mater.* 20, 1160 (2008).
6. X. S. Zhou, Y. X. Yin, L. J. Wan, and Y. G. Guo, *J. Mater. Chem.* 22, 17456 (2012).
7. L. Y. Jiang, X. L. Wu, Y. G. Guo, and L. J. Wan, *J. Phys. Chem. C* 113, 14213 (2009).
8. X. F. Li, X. B. Meng, J. Liu, D. S. Geng, Y. Zhang, N. B. Mohammad, Y. L. Li, J. L. Yang, R. Y. Li, X. L. Sun, M. Cai, and M. W. Verbrugge, *Adv. Funct. Mater.* 22, 1646 (2012).
9. D. Liu, Z. Kong, X. Liu, A. Fu, Y. Wang, Y. G. Guo, P. Guo, H. Li, and X. S. Zhao, *ACS Appl. Mater. and Interfaces* 10, 2515 (2018).
10. X. Zhou, L. J. Wan, and Y. G. Guo, *Adv. Mater.* 25, 2152 (2013).
11. Y. Wang, A. P. Fu, X. H. Liu, Y. Q. Wang, Y. H. Li, P. Z. Guo, H. L. Li, and X. S. Zhao, *J. Alloy. Compd.* 717, 341 (2017).
12. S. Stankovich, D. A. Dikin, G. H. B. Dommett, K. M. Kohlhaas, E. J. Zimney, E. A. Stach, R. D. Piner, S. T. Nguyen, and R. S. Ruoff, *Nature* 442, 282 (2006).
13. S. J. Richard Prabakar, Y. H. Hwang, E. G. Bae, S. Shim, D. Kim, M. S. Lah, K. S. Sohn, and M. Pyo, *Adv. Mater.* 25, 3307 (2013).
14. Z. T. Li, G. L. Wu, D. Liu, W. T. Wu, B. Jiang, J. Z. Zheng, Y. P. Li, J. H. Li, and M. B. Wu, *J. Mater. Chem. A* 2, 7471 (2014).
15. J. Lin, Z. Peng, C. Xiang, G. Ruan, Z. Yan, D. Natelson, and J. M. Tour, *ACS Nano.* 7, 6001 (2013).
16. C. H. Xu, J. Sun, and L. Gao, *J. Mater. Chem.* 22, 975 (2012).
17. Y. Li, X. Lv, J. Lu, and J. Li, *J. Phys. Chem. C* 114, 21770 (2010).
18. H. L. Li, H. Liu, A. P. Fu, G. L. Wu, M. Xu, G. S. Pang, P. Z. Guo, J. Q. Liu, and X. S. Zhao, *Materials* 9, 849 (2016).
19. X. Liu, X. Liu, B. Sun, H. Zhou, A. Fu, Y. Wang, Y. G. Guo, P. Guo, and H. Li, *Carbon* 130, 680 (2018).
20. A. L. Feng, G. L. Wu, C. Pan, and Y. Q. Wang, *J. Nanosci. Nanotechnol.* 17, 3786 (2017).
21. G. L. Wu, Y. H. Cheng, Z. H. Yang, Z. R. Jia, H. J. Wu, L. J. Yang, H. L. Li, P. Z. Guo, and H. L. Lv, *Chem. Eng. J.* 333, 519 (2018).
22. S. Huang, G. N. Zhu, C. Zhang, W. W. Tjju, Y. Y. Xia, and T. Liu, *ACS Appl. Mater. Interfaces* 4, 2242 (2012).
23. W. Z. Wang, C. K. Xu, G. H. Wang, Y. K. Liu, and C. L. Zheng, *J. Appl. Phys.* 92, 2740 (2002).
24. J. F. Scott, *J. Chem. Phys.* 33, 852 (1970).
25. D. N. Wang, J. L. Yang, X. F. Li, D. S. Geng, R. Y. Li, M. Cai, T. K. Sham, and X. L. Sun, *Energ. Environ. Sci.* 6, 2900 (2013).
26. L. Miao, J. B. Wu, J. J. Jiang, and P. Liang, *J. Phys. Chem. C* 117, 23 (2013).
27. D. Bresser, F. Mueller, D. Buchholz, E. Paillard, and S. Passerini, *Electrochim. Acta* 128, 163 (2014).
28. Y. X. Wang, Y. G. Lim, M. S. Park, S. L. Chou, J. H. Kim, H. K. Liu, S. H. Dou, and Y. J. Kim, *J. Mater. Chem. A* 2, 529 (2013).
29. G. L. Wu, H. J. Wu, K. K. Wang, C. H. Zheng, Y. Q. Wang, and A. L. Feng, *RSC Adv.* 6, 58069 (2016).
30. Y. Ma, B. Ding, G. Ji, and J. Y. Lee, *ACS Nano.* 7, 1087 (2013).
31. K. Shu, C. Wang, M. Wang, C. Zhao, and G. G. Wallace, *J. Mater. Chem. A* 2, 1325 (2013).
32. R. Yang, Y. G. Gu, Y. Q. Li, J. Zheng, and X. G. Li, *Acta. Mater.* 58, 866 (2010).
33. M. Zhang, D. N. Lei, X. Z. Yu, L. B. Chen, Q. H. Li, Y. G. Wang, T. H. Wang, and G. Z. Cao, *J. Mater. Chem.* 22, 23091 (2012).
34. Z. H. Wen, Q. Wang, Q. Zhang, and J. H. Li, *Adv. Funct. Mater.* 17, 2772 (2010).

Received: 1 December 2017. Accepted: 13 March 2018.